ACS OMEGA

http://pubs.acs.org/journal/acsodf

Article

Formation of Defect-Dicubane-Type $Ni^{II}_2Ln^{III}_2$ (Ln = Tb, Er) Clusters: Crystal Structures and Modeling of the Magnetic Properties

Zhonglu You, Krunoslav Prsa, Julius Mutschler, Susan N. Herringer, Jiaqi Wang, Yingying Luo, Boyang Zheng, Silvio Decurtins, Karl W. Krämer, Oliver Waldmann,* and Shi-Xia Liu*

Cite This: *ACS Omega* 2021, 6, 483−491

Read Online

ACCESS | Metrics & More | Article Recommendations | Supporting Information

ABSTRACT: In the field of molecular nanoclusters, cubane and defect-dicubane, or butterfly structures, are typical examples of tetranuclear metal core architectures. In this work, a halogenated and anionic Schiff-base ligand (L^{2-}) is utilized as it is predisposed to chelate within a cluster core to both 3d and 4f metal ions, in different binding configurations (H_2L = 4-chloro-2-(2-hydroxy-3-methoxybenzyliden amino)-phenol). The phenolate oxygen atoms of the deprotonated ligand can act in μ-O and μ_3-O bridging binding modes for the intramolecular assembly of metal ions. Based on that, two tetranuclear and isostructural compounds $[Ni_2Tb_2(L)_4(NO_3)_2(DMF)_2]\cdot 2CH_3CN$ (**1**) and $[Ni_2Er_2(L)_4(NO_3)_2(DMF)_2]\cdot 0.5CH_3CN$ (**2**) were synthesized and structurally characterized. Magnetic susceptibility and magnetization data indicate the occurrence of dominant intramolecular ferromagnetic interactions between the spin centers. Particular emphasis is given to the theoretical description of the magnetic behavior, taking into account the Ln−Ni and Ni−Ni coupling paths and the magnetic anisotropy of the Ln^{III} and Ni^{II} ions. The study is distinguished for its discussion of two distinct models, whereby model **A** relies on the uniaxial B_{20} Stevens term describing the lanthanide anisotropy and model **B** is based on point-charge model calculations. Importantly, the physical meaning of the obtained parameters for both models was critically scrutinized.

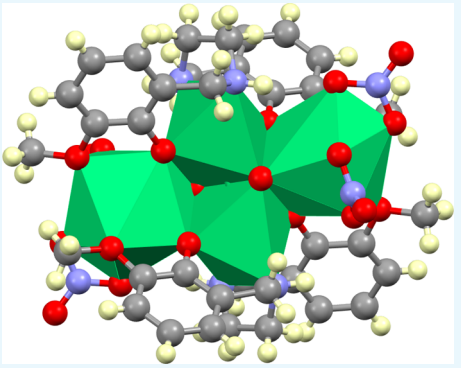

INTRODUCTION

In the field of molecular magnetism,[1−7] heteronuclear nanoclusters comprising 3d and 4f metal ions are attractive candidates for studying the factors that govern the strength and type of intracluster magnetic coupling between the metal ions.[8−30] The inherent anisotropy of the lanthanide ions and their large magnetic moments give reason to combine them with 3d metal ions, which are expected to exhibit stronger magnetic couplings. In addition, in recent decades, synthetic methods for polynuclear systems have reached a level of efficiency attained with mononuclear compounds, and consequently, the factors governing a specific core structure can often be elucidated.[31] Accordingly, a large diversity of heteronuclear structures of cluster compounds has been reported in the literature.[8−30] As a case in point, a class of π-conjugated Schiff-base ligands has been designed to be particularly suitable for assembling metal ions into a "butterfly" or defect-dicubane core structure.[24] An important property of such ligands is the availability of different coordination pockets, each of which can act as a chelating unit. Therefore, the ligands are predisposed to bond to both transition metal ions and lanthanide ions. Regarding the analysis of the magnetic properties of polynuclear coordination compounds, magneto-structural correlations are sought in order to gain insights into the pathways of the magnetic interactions. In the context of this work and to cite one example, such a correlation, which involves Ni^{II} ions, is given by relating the Ni−O−Ni angles formed *via* doubly bridged or triply bridged oxygen atoms within a cubane-type structure. For a value of this angle above 98−99°, the interaction between the Ni^{II} ions is mostly found to be of antiferromagnetic character but of ferromagnetic in the case of smaller angles.[32−34] However, one must also take into account that structural distortions within such a cluster can substantially affect these kinds of guidelines.[35]

In this paper, we report the synthesis, structure, and magnetic characterization of two tetranuclear and isostructural compounds with the stoichiometries $[Ni_2Tb_2(L)_4(NO_3)_2(DMF)_2]\cdot 2CH_3CN$ (**1**) and $[Ni_2Er_2(L)_4(NO_3)_2(DMF)_2]\cdot 0.5CH_3CN$ (**2**). Four metal ions are assembled into a defect-dicubane cluster core by four halogenated and anionic Schiff-base ligands L^{2-} (Chart 1), while nitrate anions and solvent DMF molecules complete

Received: October 9, 2020
Accepted: November 26, 2020
Published: December 21, 2020

Chart 1. Chemical Structure of the Ligand H_2L: Its Deprotonated Form L^{2-} Ligates in the Ni^{II} and Ln^{III} Ions of the Cluster Core

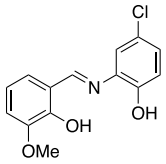

their coordination spheres. For both complexes, the magnetic susceptibility and magnetization data were experimentally determined and modeled with a critical view on the physical significance of the obtained magnetic parameters.

RESULTS AND DISCUSSION

Synthesis. The Schiff-base ligand was prepared by a condensation reaction of the corresponding aldehyde and amine in methanol. The reaction of the Schiff-base ligand with nickel acetate or nickel nitrate and rare-earth nitrate salts in a mixture of MeOH, MeCN, and DMF, in the presence of triethylamine, leads to $[Ni_2Ln_2(L)_4(NO_3)_2(DMF)_2]$ stoichiometry for the cluster compounds. Solvent DMF molecules and nitrate anions were found as terminal ligands in the coordination environment (*vide infra*). The IR data of the compounds are in agreement with their X-ray structures. The free Schiff-base features an intense band at 1638 cm^{-1}, which is attributed to the stretching vibration of the azomethine [ν(C═N)] group.[36] As a coordinated ligand, this stretching frequency appears at 1608 cm^{-1}. This downshift of the frequency indicates the coordination of the imino nitrogen to the metal atoms.

Structural Descriptions of the Complexes. The heterometallic complexes **1** and **2** crystallize in the monoclinic space groups $P2_1/n$ and $P2_1/c$, respectively. The two isostructural compounds contain a centrosymmetric $Ni_2Ln_2O_6$ cluster core with a defect-dicubane-type structure. The crystal structure of complex **1** contains two acetonitrile molecules of crystallization, while complex **2** has half of an acetonitrile molecule. The metal ions are connected by six phenolate oxygen atoms from four anionic Schiff-base ligands L^{2-}, exhibiting four μ-O and two μ_3-O binding modes (Figure 1). The bridging Ni−O−Ni angles for **1** and **2** are 97.0 and 97.1° for **1** and **2**, respectively. Figure 2 illustrates the different binding modes of the deprotonated ligands with the metal ions. Two symmetry-independent ligands L^{2-} chelate in an almost coplanar fashion to a Ni^{II} and a Tb^{III} ion from opposite sides. The O^N^O coordination pocket of one ligand binds to

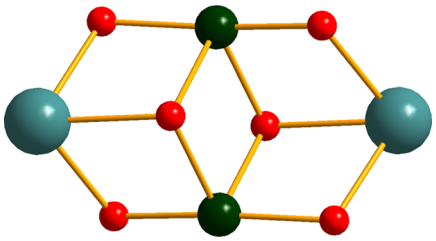

Figure 1. $Ni_2Ln_2O_6$ defect-dicubane core of **1** (Ln = Tb) and **2** (Ln = Er). Alternatively, the core structure can be described as a butterfly topology, where the two Ni^{II} ions form the body and the two Ln^{III} ions are in the wing positions (O, red; Ni, dark green; Tb, light blue).

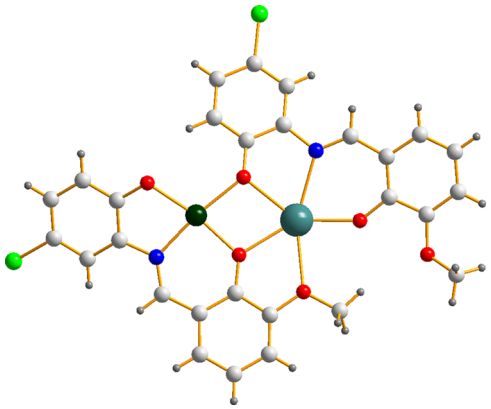

Figure 2. Fragment of complex **1** emphasizing the two symmetry-independent ligands L^{2-} with different binding modes for the Ni^{II} and Tb^{III} ions (O, red; N, blue; Cl, light green; Ni, dark green; Tb, light blue).

the Ni^{II} ion, and the same pocket of the opposite ligand binds to the Tb^{III} ion. The Tb^{III} coordination sphere is completed by the O^O coordination pocket of one ligand, which remains empty on the other ligand. Two of these fragments, related by a center of symmetry, form the cluster core (Figure 3). In the

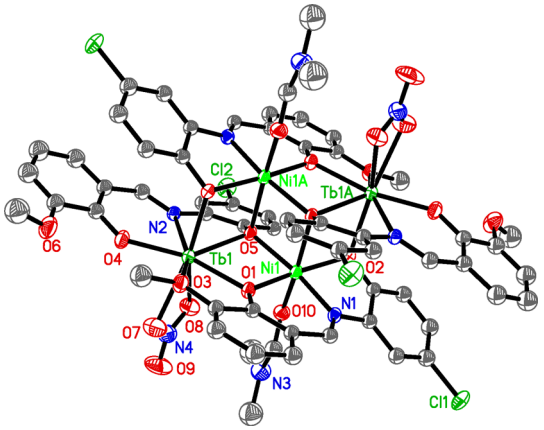

Figure 3. ORTEP structure of complex **1** drawn with 30% ellipsoid probability. Atoms labeled with the suffix A are related to the symmetry position $-x$, $1-y$, $-z$. Hydrogen atoms and the acetonitrile molecules are omitted for clarity.

cluster, the Ni^{II} ion resides in a slightly distorted octahedral NO_5 coordination geometry. The coordination sphere comprises four phenol oxygen atoms, one nitrogen atom from the chelating ligands, and one terminal monodentate DMF ligand. The Ln^{III} ion shows a distorted square antiprismatic NO_7 coordination geometry, formed by phenol oxygens, aminophenol oxygens, a methoxy oxygen, and a peripheral chelating NO_3^- ligand. Figure 3 shows the cluster of **1** (for **2**, see Figure S1), and selected bond lengths and angles for **1** and **2** are given in Table S1. Within the cluster, the aminophenol oxygens (O5) of two ligands L^{2-} form the two μ_3-O bridges, each over a Ni_2Ln triangle, and the phenol oxygens (O4) of the same Schiff-base ligate, each in a monodentate manner, to the two Ln^{III} ions. The methoxy oxygens (O6) of these two ligands remain nonbonding. The aminophenol oxygens (O2) together with the phenol oxygens (O1) of the other two ligands form the four μ-O bridges, each linking a Ni^{II} to a Ln^{III} ion, and their methoxy oxygens (O3)

https://dx.doi.org/10.1021/acsomega.0c04930
ACS Omega 2021, 6, 483−491

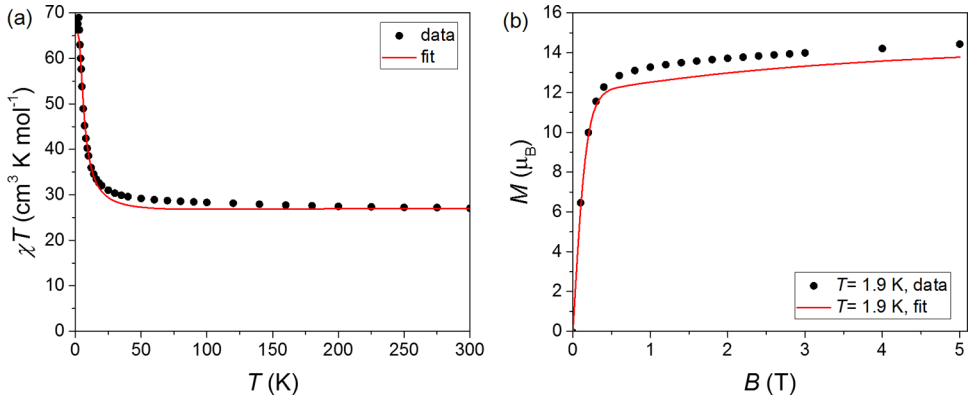

Figure 4. (a) Temperature dependence of the $\chi_M T$ product and (b) field dependence of the magnetization at 1.9 K for compound **1**. The experimental data are shown as black solid circles. The results of simultaneous fits to the data using model **A** are shown as red solid lines. The model parameters are J_{Ni} = 207(14) K, J_{Ln} = 0.67(2) K, D_{Ni} = 0.4(5) K, and χ^2 = 85.1.

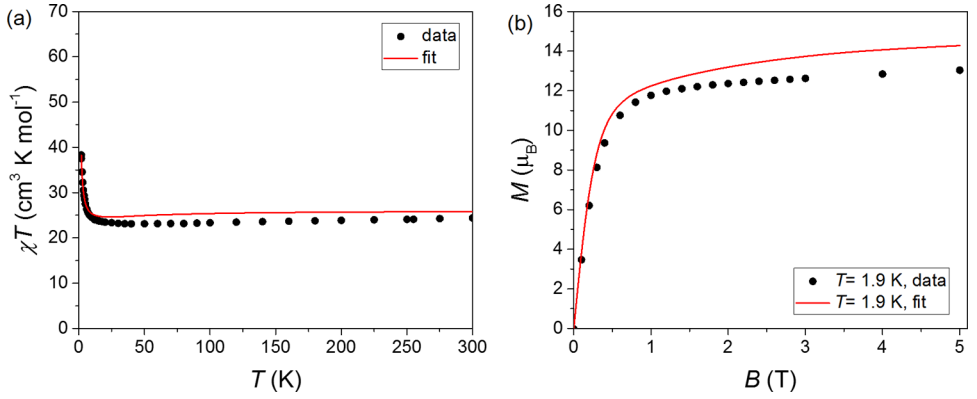

Figure 5. (a) Temperature dependence of the $\chi_M T$ product and (b) field dependence of the magnetization at 1.9 K for compound **2**. The experimental data are shown as black solid circles. The results of simultaneous fits to the data using model **A** are shown as red solid lines. The model parameters are J_{Ni} = −1.0(5) K, J_{Ln} = 0.15(2) K, D_{Ni} = −2.4(4) K, and χ^2 = 86.1.

bind monodentately to a Ln^{III} ion. The crystal packing of compounds **1** and **2** shows no special feature, and due to the bulky ligand shell around the $Ni_2Ln_2O_6$ core, the spin centers of neighboring molecules are quite distant (>9.5 Å), which minimizes any intermolecular magnetic coupling.

Magnetic Properties. The temperature dependence of the magnetic susceptibility of complexes **1** and **2** is shown in Figures 4a and 5a. At room temperature, the $\chi_M T$ products of **1** and **2** of 27.0 and 24.7 cm^3 K mol^{-1} are in good agreement with the calculated values for two independent Ni^{II} ions (S = 1 with g_{Ni} = 2) and two Tb^{III} ions ($^7F_6$) or two Er^{III} ions ($^4I_{15/2}$) of 25.6 and 25.0 cm^3 K mol^{-1}, respectively.[3] For both compounds, the $\chi_M T$ product initially does not change markedly with decreasing temperatures. Below *ca.* 10−20 K, a sharp increase in the $\chi_M T$ products is observed, which increase to 66.3 and 38.3 cm^3 K mol^{-1}, respectively, for **1** and **2**, at 1.9 K. This observation is indicative of intramolecular ferromagnetic interactions between the paramagnetic centers in each molecule. The field dependence of the magnetization at 1.9 K is shown for both compounds in Figures 4b and 5b. Up to a field of *ca.* 10 kOe, the magnetization shows a rapid increase, continues at higher fields with a slight almost linear increase, and at 50 kOe reaches values of 14.2 and 13.0 μ_B for **1** and **2**, respectively, without fully saturating. Assuming that the dominant magnetic coupling is given by the dimeric Ni^{II}_2 subunit and further considering that the increase in the $\chi_M T$ product occurs at very low temperatures, the strength of the corresponding coupling constant J_{Ni} can be of the order of only a few cm^{-1} at most.[37] The bridging Ni−O−Ni angles of 97.0 and 97.1° for **1** and **2**, respectively, are in the range where the interaction is expected to have a ferromagnetic character, in agreement with the experimental finding.[35]

The following models were considered in the analysis of the experimental magnetic data: The lanthanide magnetic moments were described by J-multiplets. The interactions involving them can thus be described by the standard Heisenberg model. The models further assume two different interaction strengths for the Ln−Ni and Ni−Ni coupling paths. The Ln−Ln interaction, due to the large separation between the ions, is expected to be small and was therefore ignored. This approximation may not be fully justified since the dipole−dipole interactions are long-range and found to be of significance in some cases for Ln^{III} ions. However, this would introduce an additional parameter, of which there are already too many in the models. The coupling scheme is depicted in Figure 6. Various models were considered, which differed in the description of the magnetic anisotropy of the Ln^{III} and Ni^{II} ions. However, we eventually settled on two models, which were exploited in detail. In model **A**, it is assumed that the uniaxial B_{20} Stevens term is the only nonzero parameter describing the lanthanide anisotropy. The model then reads

https://dx.doi.org/10.1021/acsomega.0c04930
ACS Omega 2021, 6, 483−491

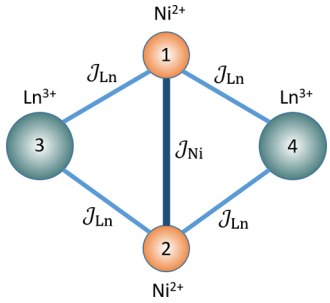

Figure 6. Assumed exchange coupling scheme for the magnetic models discussed in the text.

$$H_A = -J_{Ni}S_1S_2 - J_{Ln}(S_1 + S_2)(J_3 + J_4) + D\left[(S_1^z)^2 + (S_2^z)^2 - \frac{2}{3}\right] + \sum_{i=3,4} B_{20}O_{20}(i)$$

Here, the subscripts 1 and 2 denote the Ni^{II} spins ($S = 1$) and 3 and 4 the lanthanide magnetic moments ($J = 6$ or 15/2 for the Tb^{III} and Er^{III} magnetic moments, respectively). In the actual fitting, the model was simplified further by assuming that the B_{20} parameter is large. This effectively means that the anisotropy of the lanthanide magnetic moment is either highly Ising-like or highly XY-like.

In the second model **B**, the choice of Stevens terms for describing the lanthanide anisotropy was inspired by parameters arising from point-charge model calculations (*vide infra*). The anisotropy of the Ni^{II} ions was set to zero for simplicity. Model **B** can then be written as

$$H_B = -J_{Ni}S_1S_2 - J_{Ln}(S_1 + S_2)(J_3 + J_4) + \sum_{i=3,4} (B_{20}O_{20}(i) + B_{20}O_{22}(i) + B_{65}O_{65}(i))$$

In the actual fitting, it was further assumed that $B_{20} = B_{22}$, as also suggested by the point-charge model calculations.

In order to advance our understanding of the anisotropy of the lanthanide magnetic moment in these clusters, point-charge model (PCM) calculations of the ligand-field parameters were performed using in-house software. It is important to stress that these calculations did not aim at yielding quantitative values for the parameters of the single-ion lanthanide Hamiltonian; the PCM is usually not sufficiently accurate for such an attempt. Instead, the sole purpose of these calculations was to obtain generic information about the single-ion lanthanide spectrum and, most importantly, to hopefully identify the most relevant Stevens terms and to exclude those that do not contribute significantly. The goal of the effort was of course to overcome issues with overparametrization.

The results of the PCM calculations are expressed in terms of what we call the bare ligand-field parameters, Ω_{kl}, which are proportional to the usual Stevens parameters, B_{kl}, but are dependent on only the ligand field and not on the type of the lanthanide ion. The relationship between the B_{kl} and Ω_{kl} parameters is given as follows

$$B_{kl} = \Omega_{kl}\theta_k\frac{\langle r^k\rangle}{a_0^k}$$

Here, θ_k are the ion-dependent Stevens factors, frequently labeled in tables as α, β, and γ for $k = 2$, 4, and 6, respectively.[38] $\langle r^k\rangle$ are the ion-dependent radial averages (constants) of the *f*-electron wavefunction,[38] and a_0 is the Bohr atomic radius.

It is important to note that given the same ligand environment of the Tb^{III} and Er^{III} ions (as it can be assumed with some approximation for isostructural compounds) and due to the opposite signs of their ionic α parameters, the resulting B_{2l} parameters for these ions will be of opposite signs for equal values of the bare ligand-field parameters Ω_{2l} ($\alpha_{Tb} = -0.0101$ and $\alpha_{Er} = 0.0025$, see Table 1.4 in ref 41). Thus, if the anisotropy is of Ising-type for Tb^{III}, then it is expected to be of XY-type for Er^{III} and *vice versa*. The PCM assumed the local structure around the Ln^{III} ions based on the X-ray crystal structure data. The oxygens were modeled by charges of $-2e$ and the nitrogens by charges of $-3e$. This is certainly not a fully realistic model, but it is a reasonable attempt at getting insights into the generic trends. By means of varying the charge of the nitrogens systematically, it was confirmed that the conclusions below are representative in the sense that they are not affected by the assumed charge value.

The result of these calculations is a complex anisotropy scheme with all the possible 27 Stevens parameters present. However, for both the Er^{III} and Tb^{III} cases, the largest contributions (compared to other parameters of the same order, for example, Ω_{65} compared to Ω_{60}, and so on) are the terms $\Omega_{20} \approx \Omega_{22} = 2300$ K, $\Omega_{43} \approx -1000$ K, and $\Omega_{65} \approx 16$ K for Er^{III}, with similar values for Tb^{III} (all calculated values are listed in Table S2). This finding suggested model **B**.

For both models **A** and **B**, least-squares fits were performed using in-house software, which simultaneously included the experimental magnetization data at $T = 1.9$ K and the magnetic susceptibility data. For model **A**, the parameter B_{20} was fixed to a large value of 1500 and −1500 K for Tb^{III} and Er^{III}, respectively. The reason for this and the expected opposite sign of B_{20} has been discussed above. All other possible combinations for the sign (++, −+, and −−) were also tested but yielded worse results. The fits were reasonably fast due to the uniaxial nature of the model, which significantly simplifies the numerical averaging required for simulating powder samples (one fit by model **A** takes about four days on a modern personal computer). The best fits to the magnetic susceptibility and magnetization data using this model are shown in Figures 4 and 5. A modest agreement with experimental data is observed. While the fits for the two compounds are of the same quality, $\chi^2 \approx 85$ in both cases, the best-fit parameters for the Ni^{II} ions differ markedly and assume an unrealistically large ferromagnetic exchange value $J_{Ni} = (207 \pm 14)$ K in the Tb^{III} case and a too small value $J_{Ni} = (-1 \pm 0.5)$ K in the Er^{III} case. The large difference in the obtained J_{Ni} is noteworthy since it is not expected to differ much for the two compounds. For both compounds, reasonable and roughly consistent J_{Ln} values were obtained, $J_{Ln} = (0.67 \pm 0.02)$ K for the Tb^{III} case and $J_{Ln} = (0.15 \pm 0.02)$ K for the Er^{III} case. The anisotropy (D) of the Ni^{II} ion is zero within the uncertainty given by the fit for the Tb^{III} case, which can be considered acceptable given that the magnetic response is dominated by the larger lanthanide magnetic moments. For the Er^{III} case, $D = (-2.4 \pm 0.4)$ K was obtained. Given such differences in the parameters between the two isostructural compounds, one should not accept these results as reflecting the physical truth. It would appear more likely that two basically unrelated minima are found in a high-dimensional parameter space for the two compounds. As John von Neumann put it: "With four

https://dx.doi.org/10.1021/acsomega.0c04930
ACS Omega 2021, 6, 483−491

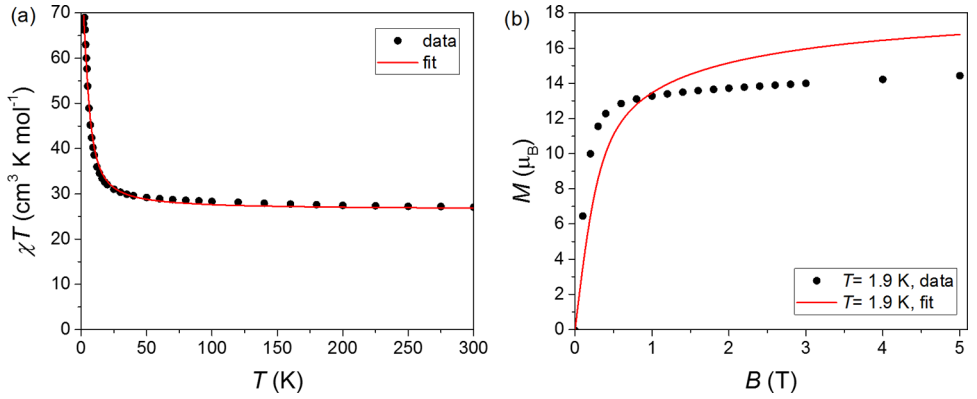

Figure 7. Results of the simultaneous fits by model **B** to (a) magnetic susceptibility and (b) magnetization data taken at 1.9 K for Tb^{III} compound **1** (black solid circles = experimental data; red solid lines = fits). The parameters are given in the text.

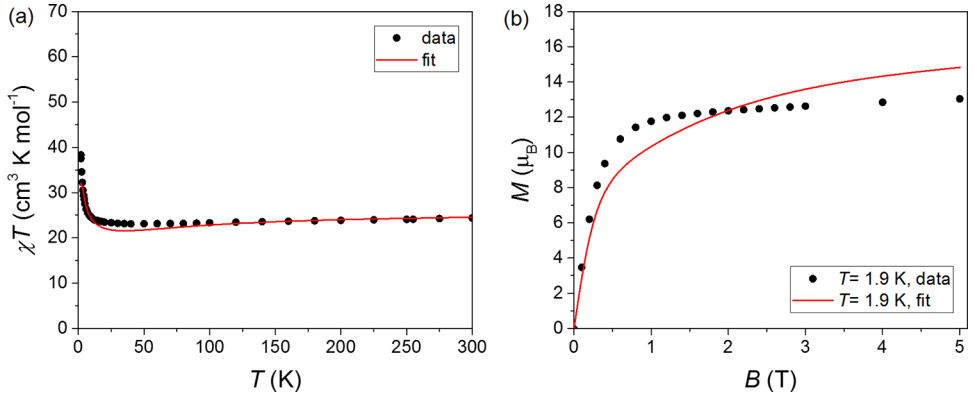

Figure 8. Results of the simultaneous fits by model **B** to (a) magnetic susceptibility and (b) magnetization data taken at 1.9 K for Er^{III} compound **2** (black solid circles = experimental data; red solid lines = fits). The parameters are given in the text.

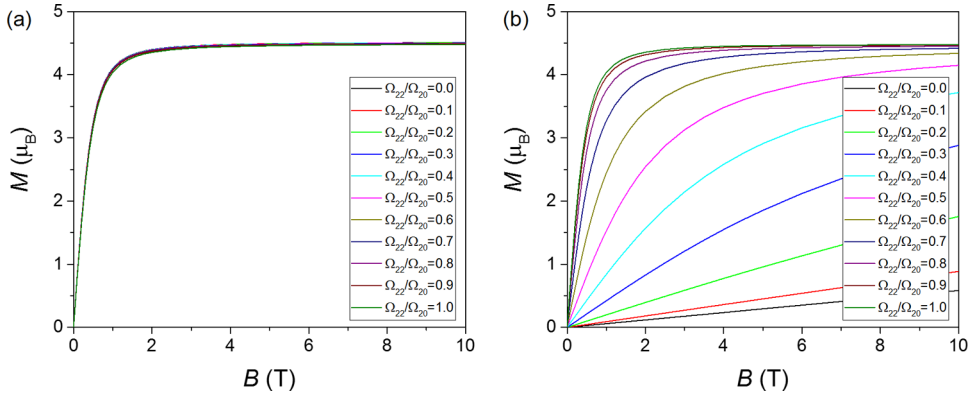

Figure 9. Single-ion magnetization calculations at T = 2 K for a Tb^{III} ion assuming (a) positive and (b) negative signs of Ω_{20} and different ratios of Ω_{22}/Ω_{20} ($|\Omega_{20}|$ = 100,000 K).

parameters I can fit an elephant, and with five I can make him even wiggle his trunk."

With regard to model **B**, the biaxial nature of the model and the required detailed powder averaging resulted in exceptionally long fit times of about 8 weeks per fit. The obtained best fits are shown in Figures 7 and 8. It is obvious that the best fits by model **B** are significantly worse than those by model **A**. The large $\chi^2 \approx 130$ for both the Tb^{III} and Er^{III} compounds confirms this. Model **B** appears to be able to reasonably reproduce the magnetic susceptibility; however, the fits for the magnetization data are systematically off. In the Tb^{III} case, a small ferromagnetic exchange $J_{Ni} = (0 \pm 2)$ K and a reasonable $J_{Ln} = (0.9 \pm 0.1)$ K were obtained. The best-fit Stevens parameters for the Tb^{III} compound are $B_{20} = B_{22} = (6 \pm 1)\cdot10^{-2}$ K and an enormously large $B_{65} = (-780 \pm 70)\cdot10^{-6}$ K. For the Er^{III} case, the best-fit exchange couplings are $J_{Ni} = (-34 \pm 1)$ K and $J_{Ln} = (3.0 \pm 0.3)$ K, and the best-fit Stevens parameters are $B_{20} = B_{22} = (25 \pm 3)\cdot10^{-2}$ K and $B_{65} = (3 \pm 1)\cdot10^{-6}$ K. One again faces the situation that the fit parameters do not resemble one another for the two compounds, and the impression of "fitting an elephant" holds for fits by model **B** as well.

In order to understand the results better, the powder averaged magnetic susceptibility and low-temperature magnetization curves were calculated assuming a single-ion lanthanide

https://dx.doi.org/10.1021/acsomega.0c04930
ACS Omega 2021, 6, 483−491

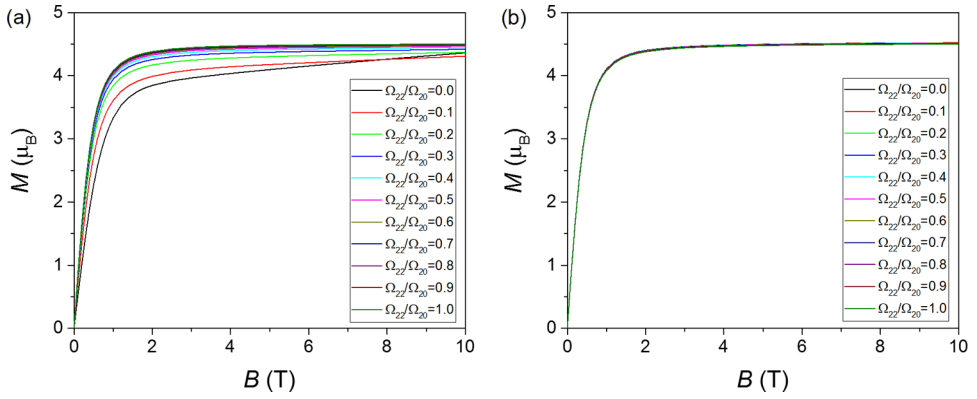

Figure 10. Single-ion magnetization calculations at T = 2 K for an Er^{III} ion assuming (a) positive and (b) negative signs of Ω_{20} and different ratios of Ω_{22}/Ω_{20} ($|\Omega_{20}|$ = 100,000 K).

cluster with only nonzero Ω_{20} and Ω_{22} parameters (which are proportional to the Stevens parameters B_{20} and B_{22}, respectively). The results for the magnetization curves at T = 2 K are shown for Tb^{III} and Er^{III} in Figures 9 and 10, respectively, for various ratios of Ω_{22}/Ω_{20}. It can clearly be seen that for the cases Tb^{III} with $\Omega_{20} > 0$ and Er^{III} with $\Omega_{20} < 0$, which corresponds to $B_{20} < 0$ and thus Ising-type anisotropy for both ions, the details of the magnetization curves are not sensitive even to the quite drastic changes of the ratio Ω_{22}/Ω_{20} and appear to show a similar, generic behavior. This is somewhat expected given that in both cases, the Ising-type anisotropy results in ground states that are largely insensitive to orthorhombic anisotropies. Interestingly, also for the Er^{III} case with $\Omega_{20} > 0$, only a weak sensitivity of the Ω_{22} parameter is obtained. Only for the Tb^{III} case with $\Omega_{20} < 0$ is a pronounced effect on Ω_{22} found. These unfortunate findings are obviously an effect of the powder averaging, which smoothens out any features that would normally be expected from single-crystal data. It is, however, also an effect of the insensitivity of magnetic data to details of the ground and excited states. Given that the above analysis indicates that $\Omega_{20} > 0$ is evident in complexes **1** and **2**, it is thus not surprising that the anisotropy parameters cannot be very well determined based on the powder magnetic data alone. On the other hand, one would then also expect that these magnetic data can be accurately described by simple models and a small parameter set. Surprisingly, this does not appear to be the case. Further investigations into this seeming contradiction should be of much interest.

CONCLUSIONS

A halogenated Schiff-base ligand L^{2-} was utilized to assemble Ni^{II} and Ln^{III} (Ln = Tb, Er) ions into a heteronuclear defect-dicubane-type structure. Magnetic properties of both isostructural cluster compounds were determined, and steps have been taken to carefully elucidate them by modeling the experimental data with different approaches. Point-charge model calculations for the lanthanide ligand-field parameters and fits for the magnetization and magnetic susceptibility data were performed. The point-charge model suggests a complex anisotropy of the lanthanide ions. Selecting the few most dominant Stevens parameters inspired model **B**, which in this sense could be viewed as a sort of a "realistic" model. In addition, model **A** was studied, which cannot be justified from the actual ligand-field environment present in the studied clusters, but was introduced merely for its simplicity and the underlying idea that the Tb^{III} ions might show a strong Ising anisotropy. Interestingly enough, fits by model **B** resulted in worse agreement with the experimental data than the simple model **A**. Normally, one would expect that the more parameters one uses in a fit, the better agreement with the data is obtained. Curiously, this does not seem to hold. It was emphasized that the large scatter in the best-fit parameters puts the physical significance of the obtained parameter values into question. Obviously, as also demonstrated by additional calculations, even coarse aspects of the anisotropy in lanthanide-containing magnetic molecules can often be washed out nearly completely in powder samples. While the effect itself is of course not surprising, the severity of the effect is somewhat surprising. Magnetization data taken on small single crystals, when available, would go a long way to discern details of the anisotropy.

EXPERIMENTAL SECTION

Materials. Starting materials, reagents, and solvents were purchased from commercial suppliers with AR grade and used as received.

General Methods. Elemental analyses were performed on a PerkinElmer 240C elemental analyzer. IR spectra were recorded on a Jasco FT/IR-4000 spectrometer as KBr pellets in the 4000−400 cm^{-1} region. UV−vis spectra were recorded on a PerkinElmer Lambda 900 spectrometer. ^1H NMR and ^{13}C NMR were performed with a Bruker 500 MHz spectrometer. Single-crystal structures were determined on a Bruker D8 Venture single-crystal diffractometer.

Synthesis of 4-Chloro-2-(2-hydroxy-3-methoxy benzyliden amino)phenol (H_2L). 3-Methoxysalicylaldehyde (0.15 g, 1.0 mmol) and 2-amino-4-chlorophenol (0.14 g, 1.0 mmol) were mixed in methanol (50 mL). The mixture was stirred for 30 min at reflux, and the solvent was evaporated by distillation. The solid was recrystallized from methanol to give an orange crystalline product. Yield: 92%. Elemental analysis (%) calcd. for $C_{14}H_{12}ClNO_3$: C, 60.55; H, 4.36; N, 5.04. Found: C, 60.41; H, 4.27; N, 5.13. IR data (cm^{-1}): 1638 (vs), 1505 (s), 1435 (w), 1347 (w), 1247 (m), 1210 (s), 1105 (w), 1068 (w), 1014 (w), 972 (w), 906 (w), 739 (m), 568 (m), 514 (m). UV−vis data in methanol (λ (nm), ε ($L{\cdot}mol^{-1}{\cdot}cm^{-1}$)): 263, 3.12 × 10;[4] 298, 1.50 × 10;[4] 345, 1.20 × 10;[4] 450, 2.45 × 10.[3] ^1H NMR (500 MHz, DMSO-d_6): 13.65 (s, 1H, O*H*), 10.01 (s, 1H, O*H*), 8.98 (s, 1H, C*H*═N), 7.48 (s, 1H, Ar*H*), 7.20 (d, J = 7.8 Hz, 1H, Ar*H*), 7.16 (d, J = 8.6 Hz, 1H, Ar*H*), 7.10 (d, J = 7.9 Hz, 1H, Ar*H*), 6.96 (d, J = 8.7 Hz, 1H, Ar*H*),

https://dx.doi.org/10.1021/acsomega.0c04930
ACS Omega 2021, 6, 483−491

6.88 (t, J = 7.9 Hz, 1H, ArH), 3.81 (s, 3H, OCH_3). ^{13}C NMR (126 MHz, DMSO-d_6): 162.94, 151.38, 150.05, 148.07, 135.91, 127.29, 123.95, 123.09, 119.21, 119.14, 118.18, 117.75, 115.56, 55.87.

Syntheses of the Complexes 1 and 2. The Schiff-base ligand H_2L (0.14 g, 0.5 mmol) was dissolved in MeOH (7.5 mL), MeCN (2.5 mL), and DMF (10 mL). Then, triethylamine (0.10 g, 1.0 mmol) was added to the solution, which was stirred at room temperature for 10 min. Then, a methanolic solution (5 mL) of $Ni(NO_3)_2{\cdot}6H_2O$ (0.15 g, 0.5 mmol) and a methanolic solution (5 mL) of $Ln(NO_3)_3{\cdot}6H_2O$ (0.5 mmol; Ln = Tb for **1**, Er for **2**) were added. The reaction mixture was further stirred for 30 min at room temperature to afford a clear brownish-green solution. The solution was allowed to slowly evaporate at room temperature for a period of a week, while well-shaped single crystals of the respective complexes were formed and collected by filtration.

*$[Ni_2Tb_2(L)_4(NO_3)_2(DMF)_2]{\cdot}2CH_3CN$ (**1**).* Yield: 37%. Elemental analysis (%) calcd. for $C_{66}H_{60}Cl_4N_{10}Ni_2O_{20}Tb_2$: C, 41.94; H, 3.20; N, 7.41. Found: C, 41.72; H, 3.28; N, 7.37. IR data (KBr, cm^{-1}): 3440 w, 3060 w, 2932 w, 2839 w, 1666 s, 1608 s, 1546 m, 1475 sh, 1447 m, 1452 sh, 1382 s, 1328 w, 1275 m, 1224 s, 1175 m, 1113 s, 1084 m, 1023 w, 973 m, 912 s, 855 m, 822 sh, 783 w, 740 s, 679 m, 596 m, 521 m, 492 m, 446 w. UV−vis data in methanol (λ, ε): 235 nm, 2.71 × 10^4 L·mol^{-1}·cm^{-1}; 309 nm, 1.16 × 10^4 L·mol^{-1}·cm^{-1}; 360 nm, 8.91 × 10^3 L·mol^{-1}·cm^{-1}; 425 nm, 9.73 × 10^3 L·mol^{-1}·cm^{-1}.

*$[Ni_2Er_2(L)_4(NO_3)_2(DMF)_2]{\cdot}0.5CH_3CN$ (**2**).* Yield: 33%. Elemental analysis (%) calcd. for $C_{63}H_{55.5}Cl_4Er_2N_{8.5}Ni_2O_{20}$: C, 41.00; H, 3.03; N, 6.45. Found: C, 41.06; H, 3.14; N, 6.34. IR data (KBr, cm^{-1}): 3450 w, 3063 w, 2934 w, 2836 w, 1663 s, 1608 s, 1550 m, 1477 sh, 1448 m, 1384 s, 1329 w, 1274 m, 1224 s, 1178 m, 1108 s, 1085 m, 1027 w, 971 m, 911 s, 861 w, 824 sh, 782 w, 737 s, 679 m, 595 m, 521 m, 445 w. UV−vis data in methanol (λ, ε): 235 nm, 2.56 × 10^4 L·mol^{-1}·cm^{-1}; 305 nm, 1.23 × 10^4 L·mol^{-1}·cm^{-1}; 375 nm, 9.37 × 10^3 L·mol^{-1}·cm^{-1}; 415 nm, 9.03 × 10^3 L·mol^{-1}·cm^{-1}.

General X-ray Crystallography. Diffraction intensities for complexes **1** and **2** were collected at 298(2) K using a Bruker D8 Venture diffractometer with Mo Kα radiation (λ = 0.71073 Å). The collected data were reduced with SAINT,[39] and multiscan absorption correction was performed using SADABS.[40] Structures of the complexes were solved by direct methods and refined against F^2 by a full-matrix least-squares method using SHELXL.[41] All of the nonhydrogen atoms were refined anisotropically. The hydrogen atoms were placed in calculated positions and constrained to ride on their parent atoms. Crystallographic data for complexes **1** and **2** are summarized in Table 1. Selected bond lengths and angles for **1** and **2** are given in Table S1.

Magnetic Measurements. Magnetic susceptibility and magnetization data were recorded for powdered samples of complexes **1** and **2** on a Quantum Design MPMS-5XL SQUID magnetometer. Magnetic susceptibility data were taken in the temperature range from 1.9 to 300 K in a magnetic field of 1 kOe. Magnetization measurements were performed at 1.9 K in magnetic fields of 0 to 50 kOe. The magnetic data were corrected for the empty sample holder and diamagnetic contributions from the sample (−0.45 × 10^{-6} cm^3/g·molar weight). Transmission powder X-ray analysis was utilized to ensure that the single-crystal data were representative of the bulk material.

Table 1. Details of the Data Collection and Refinement Parameters for Complexes 1 and 2

complex	1	2
empirical formula	$C_{66}H_{60}Cl_4N_{10}Ni_2O_{20}Tb_2$	$C_{63}H_{55.5}Cl_4N_{8.5}Ni_2O_{20}Er_2$
formula weight/ g mol^{-1}	1890.30	1845.40
temperature/K	298(2)	298(2)
wavelength/Å	0.71073	0.71073
crystal system	monoclinic	monoclinic
space group	$P2_1/n$	$P2_1/c$
a/Å	13.7343(11)	12.1038(8)
b/Å	13.7633(11)	19.1062(19)
c/Å	18.8592(12)	16.2693(15)
α/°	90	90
β/°	96.8840(10)	109.133(2)
γ/°	90	90
volume/Å^3	3539.2(5)	3554.6(5)
Z	2	2
D_c/g·cm^{-3}	1.774	1.724
μ/mm^{-1}	2.729	3.085
F(000)	1880	1826
θ limit/°	1.74−25.50	2.13−25.50
unique reflections	6593	6626
observed reflections [$I \geq 2\sigma(I)$]	4589	4833
parameters	474	469
restraints	0	18
R_{int}	0.0590	0.0564
goodness of fit on F^2	1.027	1.067
R_1, wR_2 [$I \geq 2\sigma(I)$]	0.0393, 0.0717	0.0436, 0.1078
R_1, wR_2 (all data)	0.0729, 0.0835	0.0700, 0.1239

■ ASSOCIATED CONTENT

Supporting Information

The Supporting Information is available free of charge at https://pubs.acs.org/doi/10.1021/acsomega.0c04930.

(Figure S1) Crystal structure of **2**, (Figures S2 and S3) powder X-ray diffraction patterns of **1** and **2**, (Figures S4 and S5) TG data of **1** and **2**, (Table S1) selected bond distances and angles for **1** and **2**, and (Table S2) Ω_{kl} parameters for complexes **1** and **2** (PDF)

Accession Codes

CCDC 2023185 and 2023186 contain the supplementary crystallographic data for this paper. These data can be obtained free of charge via www.ccdc.cam.ac.uk/data/cif, by emailing data_request@ccdc.cam.ac.uk, or by contacting The Cambridge Crystallographic Data Centre, 12 Union Road, Cambridge CB2 1EZ, UK; fax: +44 1223 336033.

■ AUTHOR INFORMATION

Corresponding Authors

Oliver Waldmann − *Physikalisches Institut, Universität Freiburg, Freiburg D-79104, Germany;* orcid.org/0000-0001-9967-300X; Email: oliver.waldmann@physik.uni-freiburg.de

Shi-Xia Liu − *Departement für Chemie und Biochemie, Universität Bern, Bern CH-3012, Switzerland;* orcid.org/0000-0001-6104-4320; Email: liu@dcb.unibe.ch

https://dx.doi.org/10.1021/acsomega.0c04930
ACS Omega 2021, 6, 483−491

Authors

Zhonglu You − *Department of Chemistry and Chemical Engineering, Liaoning Normal University, Dalian 116029, P. R. China*

Krunoslav Prsa − *Physikalisches Institut, Universität Freiburg, Freiburg D-79104, Germany*

Julius Mutschler − *Physikalisches Institut, Universität Freiburg, Freiburg D-79104, Germany*

Susan N. Herringer − *Departement für Chemie und Biochemie, Universität Bern, Bern CH-3012, Switzerland;* orcid.org/0000-0002-1500-8422

Jiaqi Wang − *Department of Chemistry and Chemical Engineering, Liaoning Normal University, Dalian 116029, P. R. China*

Yingying Luo − *Department of Chemistry and Chemical Engineering, Liaoning Normal University, Dalian 116029, P. R. China*

Boyang Zheng − *Department of Chemistry and Chemical Engineering, Liaoning Normal University, Dalian 116029, P. R. China*

Silvio Decurtins − *Departement für Chemie und Biochemie, Universität Bern, Bern CH-3012, Switzerland*

Karl W. Krämer − *Departement für Chemie und Biochemie, Universität Bern, Bern CH-3012, Switzerland;* orcid.org/0000-0001-5524-7703

Complete contact information is available at: https://pubs.acs.org/10.1021/acsomega.0c04930

Author Contributions

The manuscript was written through contributions of all authors. All authors have given approval to the final version of the manuscript.

Notes

The authors declare no competing financial interest.

■ ACKNOWLEDGMENTS

We are grateful to the Swiss National Science Foundation for the financial support under grant no. 200020_172659 and the High Level Cultivation Project of the Liaoning Normal University [grant no. GD19L005].

■ REFERENCES

(1) Winpenny, R. *Molecular Cluster Magnets*; World Scientific: London, 2012.

(2) Gatteschi, D.; Sessoli, R.; Villain, J. *Molecular Nanomagnets*. Oxford University Press: Oxford, U.K., 2006, DOI: 10.1093/acprof:oso/9780198567530.001.0001.

(3) Kahn, O. *Molecular Magnetism*; VCH Publishers, Inc.: New York, 1993.

(4) Sessoli, R.; Powell, A. K. Strategies towards single molecule magnets based on lanthanide ions. *Coord. Chem. Rev.* **2009**, *253*, 2328−2341.

(5) Pilkington, M.; Decurtins, S. Molecular-Based Magnetism in High-Spin Molecular Clusters and Three-Dimensional Networks Based on Cyanometalate Building Blocks. *Chimia* **2000**, *54*, 593−601.

(6) Sorace, L.; Benelli, C.; Gatteschi, D. Lanthanides in molecular magnetism: old tools in a new field. *Chem. Soc. Rev.* **2011**, *40*, 3092−3104.

(7) Decurtins, S.; Pellaux, R.; Hauser, A.; von Arx, M. E. Solid state supramolecular chemistry of oxalato-bridged transition-metal compounds with two- and three-dimensional connectivities − structure, magnetism and photophysics. In *Magnetism: A supramolecular Function*, Kahn, O., Ed. Kluwer Academic Publishers: Dordrecht, 1996; Vol. *C-484* pp. 487−508.

(8) Dey, A.; Acharya, J.; Chandrasekhar, V. Heterometallic 3d−4f Complexes as Single-Molecule Magnets. *Chem. − Asian J.* **2019**, *14*, 4433−4453.

(9) Piquer, L. R.; Sañudo, E. C. Heterometallic 3d-4f single-molecule magnets. *Dalton Trans.* **2015**, *44*, 8771−8780.

(10) Langley, S. K.; Wielechowski, D. P.; Vieru, V.; Chilton, N. F.; Moubaraki, B.; Chibotaru, L. F.; Murray, K. S. Modulation of slow magnetic relaxation by tuning magnetic exchange in {Cr2Dy2} single molecule magnets. *Chem. Sci.* **2014**, *5*, 3246−3256.

(11) Polyzou, C. D.; Efthymiou, C. G.; Escuer, A.; Cunha-Silva, L.; Papatriantafyllopoulou, C.; Perlepes, S. P. In search of 3d/4f-metal single-molecule magnets: Nickel(II)/lanthanide(III) coordination clusters. *Pure Appl. Chem.* **2013**, *85*, 315−327.

(12) Andruh, M.; Costes, J.-P.; Diaz, C.; Gao, S. 3d−4f Combined Chemistry: Synthetic Strategies and Magnetic Properties. *Inorg. Chem.* **2009**, *48*, 3342−3359.

(13) Vieru, V.; Pasatoiu, T. D.; Ungur, L.; Suturina, E.; Madalan, A. M.; Duhayon, C.; Sutter, J.-P.; Andruh, M.; Chibotaru, L. F. Synthesis, Crystal Structures, Magnetic Properties, and Theoretical Investigation of a New Series of Ni^{II}−Ln^{III}−W^{V} Heterotrimetallics: Understanding the SMM Behavior of Mixed Polynuclear Complexes. *Inorg. Chem.* **2016**, *55*, 12158−12171.

(14) Radu, I.; Kravtsov, V. C.; Krämer, K.; Decurtins, S.; Liu, S.-X.; Reu, O. S.; Ostrovsky, S. M.; Klokishner, S. I.; Baca, S. G. Synthesis, Characterization, and Modeling of Magnetic Properties of a Hexanuclear Amino Alcohol-Supported {CoII2CoIII2DyIII2} Pivalate Cluster. *J. Phys. Chem. C* **2016**, *120*, 7435−7443.

(15) Zou, H.-H.; Sheng, L.-B.; Liang, F.-P.; Chen, Z.-L.; Zhang, Y.-Q. Experimental and theoretical investigations of four 3d−4f butterfly single-molecule magnets. *Dalton Trans.* **2015**, *44*, 18544−18552.

(16) Moreno Pineda, E.; Chilton, N. F.; Tuna, F.; Winpenny, R. E. P.; McInnes, E. J. L. Systematic Study of a Family of Butterfly-Like {M2Ln2} Molecular Magnets (M = MgII, MnIII, CoII, NiII, and CuII; Ln = YIII, GdIII, TbIII, DyIII, HoIII, and ErIII). *Inorg. Chem.* **2015**, *54*, 5930−5941.

(17) Langley, S. K.; Le, C.; Ungur, L.; Moubaraki, B.; Abrahams, B. F.; Chibotaru, L. F.; Murray, K. S. Heterometallic 3d−4f Single-Molecule Magnets: Ligand and Metal Ion Influences on the Magnetic Relaxation. *Inorg. Chem.* **2015**, *54*, 3631−3642.

(18) Goura, J.; Guillaume, R.; Rivière, E.; Chandrasekhar, V. Hexanuclear, Heterometallic, Ni_3Ln_3 Complexes Possessing O-Capped Homo- and Heterometallic Structural Subunits: SMM Behavior of the Dysprosium Analogue. *Inorg. Chem.* **2014**, *53*, 7815−7823.

(19) Langley, S. K.; Wielechowski, D. P.; Vieru, V.; Chilton, N. F.; Moubaraki, B.; Abrahams, B. F.; Chibotaru, L. F.; Murray, K. S. A {CrIII2DyIII2} Single-Molecule Magnet: Enhancing the Blocking Temperature through 3d Magnetic Exchange. *Angew. Chem., Int. Ed.* **2013**, *52*, 12014−12019.

(20) Chesman, A. S. R.; Turner, D. R.; Berry, K. J.; Chilton, N. F.; Moubaraki, B.; Murray, K. S.; Deacon, G. B.; Batten, S. R. LnIII2MnIII2 heterobimetallic "butterfly" complexes displaying antiferromagnetic coupling (Ln = Eu, Gd, Tb, Er). *Dalton Trans.* **2012**, *41*, 11402−11412.

(21) Costes, J.-P.; Dahan, F.; Vendier, L.; Shova, S.; Lorusso, G.; Evangelisti, M. Ni^{II}−Ln^{III} complexes with o-vanillin as the main ligand: syntheses, structures, magnetic and magnetocaloric properties. *Dalton Trans.* **2018**, *47*, 1106−1116.

(22) Radu, I.; Kravtsov, V. C.; Ostrovsky, S. M.; Reu, O. S.; Krämer, K.; Decurtins, S.; Liu, S.-X.; Klokishner, S. I.; Baca, S. G. Tetranuclear {CoII2CoIII2}, Octanuclear {CoII4CoIII4}, and Hexanuclear {CoIII3DyIII3} Pivalate Clusters: Synthesis, Magnetic Characterization, and Theoretical Modeling. *Inorg. Chem.* **2017**, *56*, 2662−2676.

(23) Colacio, E.; Ruiz, J.; Mota, A. J.; Palacios, M. A.; Cremades, E.; Ruiz, E.; White, F. J.; Brechin, E. K. Family of Carboxylate- and Nitrate-diphenoxo Triply Bridged Dinuclear $Ni^{II}Ln^{III}$ Complexes (Ln = Eu, Gd, Tb, Ho, Er, Y): Synthesis, Experimental and Theoretical

Magneto-Structural Studies, and Single-Molecule Magnet Behavior. *Inorg. Chem.* **2012**, *51*, 5857−5868.
(24) Mondal, K. C.; Kostakis, G. E.; Lan, Y.; Wernsdorfer, W.; Anson, C. E.; Powell, A. K. Defect-Dicubane Ni2Ln2 (Ln = Dy, Tb) Single Molecule Magnets. *Inorg. Chem.* **2011**, *50*, 11604−11611.
(25) Sutter, J.-P.; Dhers, S.; Rajamani, R.; Ramasesha, S.; Costes, J.-P.; Duhayon, C.; Vendier, L. Hetero-Metallic {3d-4f-5d} Complexes: Preparation and Magnetic Behavior of Trinuclear [(LMe2Ni−Ln){W(CN)8}] Compounds (Ln = Gd, Tb, Dy, Ho, Er, Y; LMe2 = Schiff base) and Variable SMM Characteristics for the Tb Derivative. *Inorg. Chem.* **2009**, *48*, 5820−5828.
(26) Chandrasekhar, V.; Pandian, B. M.; Vittal, J. J.; Clérac, R. Synthesis, Structure, and Magnetism of Heterobimetallic Trinuclear Complexes {[L2Co2Ln][X]} [Ln = Eu, X = Cl; Ln = Tb, Dy, Ho, X = NO3; LH3 = (S)P[N(Me)N═CH−C6H3-2-OH-3-OMe]3]: A 3d−4f Family of Single-Molecule Magnets. *Inorg. Chem.* **2009**, *48*, 1148−1157.
(27) Darii, M.; Kravtsov, V. C.; Krämer, K.; Hauser, J.; Decurtins, S.; Liu, S.-X.; Affronte, M.; Baca, S. G. Aggregation of a Giant Bean-like $\{Mn_{26}Dy_6\}$ Heterometallic Oxo-Hydroxo-Carboxylate Nanosized Cluster from a Hexanuclear {Mn6} Precursor. *Cryst. Growth Des.* **2020**, *20*, 33−38.
(28) Botezat, O.; van Leusen, J.; Hauser, J.; Decurtins, S.; Liu, S.-X.; Kögerler, P.; Baca, S. G. A Spontaneous Condensation Sequence from a {Fe6Dy3} Wheel to a {Fe7Dy4} Globe. *Cryst. Growth Des.* **2019**, *19*, 2097−2103.
(29) Shiga, T.; Onuki, T.; Matsumoto, T.; Nojiri, H.; Newton, G. N.; Hoshino, N.; Oshio, H. Undecanuclear mixed-valence 3d−4f bimetallic clusters. *Chem. Commun.* **2009**, 3568−3570.
(30) Mishra, A.; Wernsdorfer, W.; Parsons, S.; Christou, G.; Brechin, E. K. The search for 3d−4f single-molecule magnets: synthesis, structure and magnetic properties of a $[Mn^{III}_2Dy^{III}_2]$ cluster. *Chem. Commun.* **2005**, 2086−2088.
(31) Isele, K.; Franz, P.; Ambrus, C.; Bernardinelli, G.; Decurtins, S.; Williams, A. F. Self-Assembly and Interconversion of Tetranuclear Copper(II) Complexes. *Inorg. Chem.* **2005**, *44*, 3896−3906.
(32) Torić, F.; Pavlović, G.; Pajić, D.; Hrenar, T.; Zadro, K.; Cindrić, M. Tetranuclear dicubane Ni(II) complexes with antiferromagnetically interacting Ni(II) ions: Solvothermal synthesis and magneto-structural study. *Inorg. Chim. Acta* **2019**, *484*, 457−463.
(33) Clemente-Juan, J. M.; Chansou, B.; Donnadieu, B.; Tuchagues, J.-P. Synthesis, Structure, and Magnetic Properties of the Low-Symmetry Tetranuclear Cubane-like Nickel Complex [Ni4-(pypentO)(pym)(μ3-OH)2(μ-Oac)2(NCS)2(OH2)]. *Inorg. Chem.* **2000**, *39*, 5515−5519.
(34) Halcrow, M. A.; Sun, J.-S.; Huffman, J. C.; Christou, G. Structural and Magnetic Properties of [Ni4(.mu.3-OMe)4(dbm)4-(MeOH)4] and [Ni4(.eta.1,.mu.3-N3)4(dbm)4(EtOH)4]. Magneto-structural Correlations for [Ni4X4]4+ Cubane Complexes. *Inorg. Chem.* **1995**, *34*, 4167−4177.
(35) Isele, K.; Gigon, F.; Williams, A. F.; Bernardinelli, G.; Franz, P.; Decurtins, S. Synthesis, structure and properties of {M4O4} cubanes containing nickel(ii) and cobalt(ii). *Dalton Trans.* **2007**, 332−341.
(36) Surati, K. R.; Thaker, B. T. Synthesis, spectral, crystallography and thermal investigations of novel Schiff base complexes of manganese (III) derived from heterocyclic β-diketone with aromatic and aliphatic diamine. *Spectrochim. Acta A* **2010**, *75*, 235−242.
(37) Liu, S.-X.; Ambrus, C.; Dolder, S.; Neels, A.; Decurtins, S. A Dinuclear Ni(II) Complex with Two Types of Intramolecular Magnetic Couplings: Ni(II)−Ni(II) and Ni(II)−TTF•+. *Inorg. Chem.* **2006**, *45*, 9622−9624.
(38) Jensen, J.; Mackintosh, A. R. *Rare Earth Magnetism*; Clarendon Press: Oxford, U.K., 1991.
(39) Bruker AXS. *Bruker SMART (Version 5.628) and SAINT (Version 6.02)*; Bruker AXS Inc.: Madison, Wisconsin, USA 1998.
(40) Sheldrick, G. M.. *Program for Empirical Absorption Correction of Area Detector*; University of Göttingen: Germany, 1996.
(41) Sheldrick, G. M. *SHELXT, version 6.12*; BrukerAXS Inc.: Madison, WI, 2001.

https://dx.doi.org/10.1021/acsomega.0c04930
ACS Omega 2021, 6, 483−491